Journal of Sound and Vibration (1997) **202**(1), 1–27

THE INTERACTION OF PERTURBED VORTEX RINGS AND ITS SOUND GENERATION

R. C. K. Leung and N. W. M. Ko

Department of Mechanical Engineering, The University of Hong Kong, Hong Kong

(*Received* 5 *February* 1996, *and in final form* 6 *August* 1996)

Interactions of two coaxial vortex rings of thin cores with and without azimuthal instability and the far field sound radiated have been studied numerically using the vortex blob method and acoustic analogy. The azimuthal instability waves of wavenumbers $1 \leqslant m \leqslant 5$ are represented by weak axial and radial sinusoidal perturbations. It was found that the behaviour and the far field sound radiated of two perturbed vortices during the three slip throughs of $3 \leqslant m \leqslant 4$ and during the first slip through of $1 \leqslant m \leqslant 5$ are the same as those of unperturbed case $m = 0$. Because of their mutual induction, an unstable mode of the trailing vortex is found during the third slip through at $m = 1$ and 5, significantly lower wavenumbers compared with those of a single vortex ring. The far field sound radiated and their directivity, though still quadrupole, are different from those of unperturbed cases, showing the effect of perturbation on the interaction of the two vortices. A criterion for the onset of unstable mode is also established.

1. INTRODUCTION

In free shear flows, such as those of a jet, the existence of coherent structures and their interactions had been subjected to numerous studies [1–5]. The roll-up of the nozzle boundary layer into a stream of coaxial ring vortices [2], their pairing and their eventual breakdown further downstream are the basic mechanism for the jet development. Vortex pairing or coalescence denotes the tendency of the cores of a pair of vortex rings or coherent structures to rotate about each other without mutual contact [6]. However, several types of vortex pairing can occur [7], namely, the mutual slip through process [8], the vortex ring coalescence through which two initially separated vortex rings merge to form a single structure during the slip through process [2], the incomplete slip through process in which one of the cores is severely deformed before slipping through the outer [9] and the partial coalescence in which part of the fluid in the core of the leading vortex ring is entrained by the stronger trailing vortex ring [10].

The role of coherent structures and their interactions in the generation of sound had also been subjected to detailed studies [11–17]. The modelling of coherent structures as vortices with core boundaries outside which vorticity vanishes allowed the analytical study of Möhring [12] and the numerical study of Kambe and Minota [15] on the sound generated by the vortex ring interaction with slip through process. The recent theoretical and experimental study of Tang and Ko [17] showed the importance of acceleration and deceleration of the thin vortex ring elements during pairing in the production of sound. Based on the method of contour dynamics [18], the more recent study of relatively thicker vortex rings of Tang and Ko [7] showed numerically the occurrence of the different types of vortex pairing, such as the slip through process, incomplete slip through, coalescence and partial coalescence. It is also found that the radial accelerations and the rate of change

0022–460X/97/160001 + 27 $25.00/0/sv960828

of streamwise accelerations of the vorticity centroids of the vortex rings are important in the generation of sound during the interaction.

The above theoretical and numerical studies of the role of coherent structures and their interactions were based on the planar ring vortices, without azimuthal instability. However, azimuthal instability of the ring vortices, even before their interaction, was observed in flow visualization studies [5, 19–22]. Widnall and Sullivan [19] used a linear heuristic inviscid model to predict the growth of weak azimuthal waves on a single vortex ring. Recently, a three-dimensional vortex method, based on the discretization of the vorticity field into vortex vector elements of finite spherical cores, was developed [23]. The linear growth of the azimuthal instability wave and the shape of a single vortex ring agree with experimental data. In addition, Shariff *et al*. [24] considered the viscous effect and investigated the early non-linear development of a single vortex ring. The three dimensionality of the instability wave was shown to trigger the non-linear development and the formation of turbulent vortex rings.

Besides the occurrence of azimuthal waves on the initial vortex rings very near the nozzle exit, azimuthal waves also appear on the coherent structures near the end of potential core of a jet [5, 17, 20, 25]. The breakdown model of the perturbation wave along the peripheral of a ring structure under the kind of instability proposed by Widnall and Sullivan [19] into substructures also suggested the sound produced is dominated by that associated with acceleration and deceleration of the vortical filaments of the ring [17]. The sound produced under the perturbation wave development is of second order.

Although azimuthal instability had been allowed in the theoretical studies of a single ring vortex [9, 23], study on two interacting ring vortices with azimuthal instability on their circumferences is still lacking. The breakdown model of Tang and Ko [17] near the end of the potential core only concerned a single structure. Thus, the present study was aimed to investigate the flow dynamics of two weakly perturbed vortex rings during pairing. Based on the three-dimensional vortex blob method of Knio and Ghoniem [23], the effects of azimuthal instability and perturbation on the growth and shapes of the two pairing vortices under the slip through process were investigated. Further, the sound generated by these two interacting vortices was also considered.

2. MATHEMATICAL FORMULATION

2.1. VORTEX MOTION

For a constant density fluid the vorticity equation [26] is

$$\mathrm{D}\omega/\mathrm{D}t = \partial\omega/\partial t + (\mathbf{u}\cdot\nabla)\boldsymbol{\omega} = (\boldsymbol{\omega}\cdot\nabla)\mathbf{u} + \frac{1}{R_e}\nabla^2\omega, \tag{1}$$

where $\mathbf{u}$ is the fluid, $\boldsymbol{\omega} = \nabla\times\mathbf{u}$, the Reynolds number $R_e = U_0L_0/\nu$, U_0 the characteristic velocity, L_0 the characteristic length and ν the kinematic viscosity. For inviscid flow, the evolution equation for a material line element δs [26] is

$$\frac{\mathrm{D}\delta s}{\mathrm{Dt}} = \frac{\partial}{\partial t}\delta s + (\mathbf{u}\cdot\nabla)\delta s = (\delta s\cdot\nabla)\mathbf{u}. \tag{2}$$

It follows that for inviscid flow, vortex lines move as material lines (Helmholtz) and the vortex lines could be followed in a Lagrangian framework.

The velocity $\mathbf{u}$ may be decomposed into two components, namely a solenoidal $\mathbf{u}_\omega$ and an irrotational $\mathbf{u}_p$. Provided that the vorticity field is known, $\boldsymbol{\omega} = \nabla\times\mathbf{u}$ may be readily inverted to construct the velocity field. In the case of concentrated vorticity distributed

along a cluster of thin filaments, i.e., line vortices, the solenoidal velocity $\mathbf{u}_w$ induced at a point of $\mathbf{y}$ is evaluated by the Biot-Savart Law,

$$\mathbf{u}_\omega(\mathbf{y}, t) = \sum_\alpha \int_\alpha \frac{\Gamma_\alpha}{4\pi} \frac{\partial \mathbf{Y}(\xi_\alpha, t)}{\partial \xi_\alpha} \times \frac{\mathbf{y}(t) - \mathbf{Y}(\xi_\alpha, t)}{|\mathbf{y}(t) - \mathbf{Y}(\xi_\alpha, t)|^3} \, \mathrm{d}\xi_a, \tag{3}$$

where Γ_α is the circulation, $\mathbf{Y}(\xi_\alpha, t)$ is a fluid particle on the vortex filament α and ξ_α is a parametric co-ordinate along it. The integrand of Equation (3) becomes singular as $\mathbf{y} \to \mathbf{Y}(\xi_\alpha)$, since the velocity of a vortex filament of non-vanishing curvature and zero cross-section is infinite. Therefore, a cut-off or smoothing operation is applied when Equation (3) is used to compute the induced velocity from very close vortex filaments. From the physical point of view such an operation allows a finite core of a vortex filament. The irrotational velocity $\mathbf{u}_p$, which could be expressed as a scalar potential, may be uniquely determined in order to satisfy the associated boundary conditions.

In the present investigation each thin perturbed vortex ring is approximated by a vortex filament. This approximation ignores the detailed changes on vortex core and gives only the global behaviour of the vortex system. No swirl is assumed along each vortex filament. It has been shown by Moore and Saffman [27] that swirling velocity is produced to redistribute the filament volume when there are inhomogeneities. The timescale of redistribution is much smaller than that needed by the vortex filament to move significantly and the redistribution can be thought of as almost instantaneous. Thus, the vortex core size can be considered effectively unchanged. Initially, each perturbed vortex ring is taken to be,

$$\mathbf{Y} = (R + \rho_r \, \mathrm{e}^{\mathrm{i}m\theta})\mathbf{e}_r + (z + \rho_z \, \mathrm{e}^{\mathrm{i}m\theta})\mathbf{e}_z, \tag{4}$$

where $\mathbf{e}_r$ and $\mathbf{e}_z$ are unit vectors in the radial and streamwise directions, θ is the azimuthal angle, R is the radius of an unperturbed ring, z is the initial streamwise distance from a reference frame and m is the integer wavenumber of complete waves along the filament

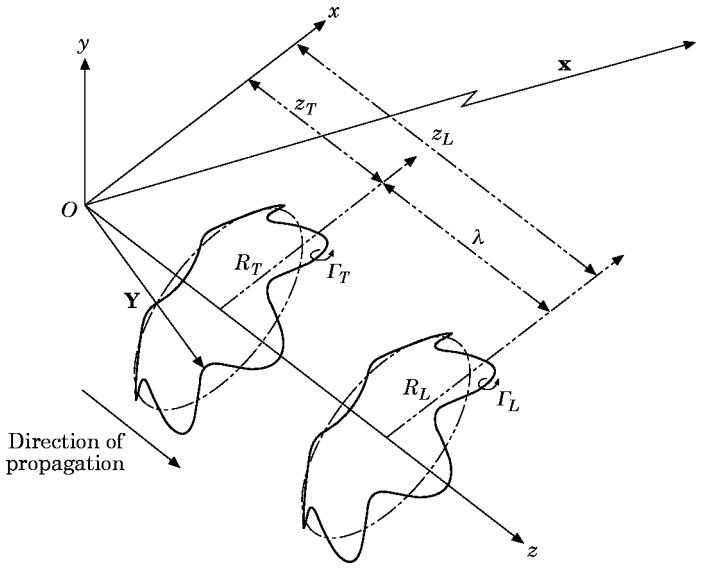

Figure 1. Schematic diagram of two perturbed vortex rings of thin cores.

periphery (Figure 1). The respective radial and streamwise perturbation amplitudes, ρ_r and ρ_z are assumed very small compared with the ring radius, i.e., $|\rho_r|$, $|\rho_z| \ll R$.

Because of mutual interaction, due to the presence of the other vortex ring, the perturbed vortex rings no longer preserve their shapes as they convect downstream. It is convenient to specify the vortex ring equivalent of a perturbed ring, which is defined as a vortex ring having identical linear hydrodynamic impulse **I** [28] to its perturbed counterpart, to depict the motions. The streamwise position z_{CA} and radius r_{CA} are constructed in accordance with the formulae of Batchelor [26] and Saffman [28] as:

$$(0, 0, z_{CA}) = \frac{1}{2}\oint \Gamma \frac{\mathbf{y}(s)(\partial \mathbf{y}(s)/\partial s)}{|\mathbf{I}|^2} \cdot \mathbf{I}\mathbf{y}(s)\, \mathrm{d}s \qquad \text{and} \qquad |\mathbf{I}| = \pi r_{CA}^2 \Gamma. \tag{5}$$

In the case of unperturbed vortex rings, z_{CA} and r_{CA} reduce to the streamwise position and radius of the vortices. As the z_{CA} and r_{CA} average out the details of the vortices during their interaction, they only indicate the global trend of the rings. The velocity V_{CA} and acceleration æ_{CA} are calculated by differentiating Equation (5) with respect to time,

$$V_{CA} = (V_z, V_r) = (\mathrm{d}/\mathrm{d}t)(z_{CA}, r_{CA}), \qquad \text{æ}_{CA} = (\text{æ}_z, \text{æ}_r) = (\mathrm{d}^2/\mathrm{d}t^2)(z_{CA}, r_{CA}). \tag{6}$$

2.2. VORTEX SOUND

The far field wave equation for low Mach number flow is

$$\nabla^2 p - (1/c_0^2)(\partial^2 p/\partial t) = -\rho_0 \nabla \cdot (\boldsymbol{\omega} \times \mathbf{u}),$$

where p, c_0 and ρ_0 denote the far field pressure, the ambient speed of sound and density of the medium respectively [11]. Möhring [12] introduces an integral formulation for the far field sound pressure fluctuations p at a point of **x** in the form of linearity in vorticity and retarded time $\tau = (t - |\mathbf{x}|/c_0)$,

$$p(\mathbf{x}, t) = \frac{\rho_0}{12\pi c_0^2 |\mathbf{x}|^3} \frac{\partial^3}{\partial t^3} \int \Gamma(\mathbf{x} \cdot \mathbf{y})\mathbf{y} \cdot (\mathrm{d}s(\mathbf{y}, \tau) \times \mathbf{x}), \tag{7}$$

where **x** and **y** denote the position vectors of a point in the far and near fields respectively and $\boldsymbol{\omega}\, \mathrm{d}^3\mathbf{y} = \Gamma\, \mathrm{d}s$. Γ is the circulation and $\mathrm{d}s$ a line element in the tangential direction on a vortex filament. The linearity of Equation (7) permits the sound field emitted by a cluster of vortex filaments and is simply the sum of their individual contributions. For two identical thin vortex rings moving along a common axis parallel to unit vector **n**, Equation (7) takes the form,

$$p(\mathbf{x}, t) = \frac{\rho_0}{4c_0^2 |\mathbf{x}|^3} \frac{\mathrm{d}^3}{\mathrm{d}t^3} \{\Gamma(R_1^2 z_1 + R_2^2 z_2)\} \mathbf{x} \cdot (\mathbf{nn} - \tfrac{1}{3}) \cdot \mathbf{x}. \tag{8}$$

Equation (8) shows the directivity of the far field is quadrupole in nature.

3. NUMERICAL METHOD

3.1. VORTEX BLOB METHOD

The motion of the perturbed vortex rings is numerically simulated, mainly based on the three dimensional vortex method of Knio and Ghoniem [23] and Winckelmans and Leonard [29]. A vortex vector element carries an amount of vorticity distributed within an associated volume. For the interaction of two vortex rings, the vorticity distribution of a vortex vector element is prescribed by a smoothing function suggested by Winckelmans and Leonard [29]. The smoothing function inhibits the singularity at the

vortex element centre and should converge to the Dirac delta function as the element size diminishes to zero. The above methods have been used to study the evolution of vortical structures, as the structures are readily approximated by a cluster of overlapping vortex vector elements [23, 29].

The vorticity field of each vortex filament is discretized into a collection of vortex vector elements or vortex blobs, which are chosen to lie on the filaments [23, 39] and is in the following form,

$$\boldsymbol{\omega}(\mathbf{y}, t) = \sum_{\alpha} \Gamma_{\alpha} \delta s_{\alpha} \zeta_{\sigma}(\mathbf{y} - \mathbf{y}_{\alpha}(t)), \tag{9}$$

where Γ_{α} is the circulation, $\mathbf{y}_{\alpha}$ the centre and δs_{α} the vector length of the vortex vector element α. For a thin core vortex, they are the corresponding values of the vortex filament [23]. The appropriate error norms for convergence of the vorticity and velocity fields go to zero as the number of vortex vector elements is increased and the core radius σ is decreased, subject to the constraint that cores overlap (i.e., $\sigma/h > 1$, where h is a typical distance between neighbouring vortex vector elements) [29]. The spherically symmetric smoothing function ζ_{σ}, with a core radius σ is constructed in the form,

$$\zeta_{\sigma}(\mathbf{y}) = (1/\sigma^3)\zeta(|\mathbf{y}|/\sigma) \tag{10}$$

with the three dimensional normalization

$$4\pi \int_0^{\infty} \zeta(\eta)\eta^2 \, \mathrm{d}\eta = 1. \tag{11}$$

During computation, σ is taken as the physical core radius of the vortex ring. Because of its simpler form together with good convergence properties, the high order algebraic smoothing proposed by Winckelmans and Leonard [29]

$$\zeta(\eta) = (15/8\pi)\,(1/(\eta^2 + 1)^{7/2}) \tag{12}$$

is adopted.

Incorporating the discretized vorticity into Equation (3) and performing the integration yield a discretized version of Bio-Savart Law,

$$\mathbf{u}_{\omega}(\mathbf{y}, t) = -\frac{1}{4\pi} \sum_{\alpha} / \Gamma_{\alpha} \frac{(\mathbf{y} - \mathbf{y}_{\alpha}) \times \delta s_{\alpha}}{|\mathbf{y} - \mathbf{y}_{\alpha}|^3} \chi\left(\frac{|\mathbf{y} - \mathbf{y}_{\alpha}|}{\delta}\right), \tag{13}$$

where

$$\chi(r) = 4\pi \int_0^{r} \xi(\eta)\eta^2 \, \mathrm{d}\eta = \frac{1}{4\pi} \frac{r^3(r^2 + 5/2)}{(r^2 + 1)^{5/2}}, \tag{14}$$

reference [29]. Equations (1) and (2) reveal the vortex filaments are being tilted and stretched by the evolving local velocity gradient $\mathbf{Vu}$. Such a vorticity stretching effect is evaluated by differentiating the expression in Equation (13) and takes the form [29],

$$\frac{\mathrm{D}\delta s_{\alpha}}{\mathrm{D}t} = \frac{1}{4\pi} \sum_{\alpha \neq \beta} \Gamma_{\alpha}\Gamma_{\beta} \left\{ -\frac{|\mathbf{r}_{\alpha\beta}|^2 + \frac{5}{2}\sigma_{\beta}^2}{(|\mathbf{r}_{\alpha\beta}|^2 + \sigma_{\beta}^2)^{5/2}} (\delta s_{\alpha} \times \delta s_{\beta}) + 3(\delta s_{\alpha} \cdot \mathbf{r}_{\alpha\beta}) \frac{|\mathbf{r}_{\alpha\beta}|^2 + \frac{7}{2}\sigma_{\beta}^2}{(|\mathbf{r}_{\alpha\beta}|^2 + \sigma_{\beta}^2)^{7/2}} (\mathbf{r}_{\alpha\beta} \times \delta s_{\beta}) \right\}, \tag{15}$$

where $\mathbf{r}_{\alpha\beta} = \mathbf{y}_{\alpha} - \mathbf{y}_{\beta}$, and σ_{β} the smoothing function core radius.

The Möhring's sound pressure fluctuation formulation is discretized in a similar manner. Substituting the discretized vorticity Equation (9) into Equation (7) gives

$$p(\mathbf{x}) = \frac{\rho_0}{12\pi c_0^2 |\mathbf{x}|^3} \frac{\partial^3}{\partial t^3} \left\{ \sum_\alpha \Gamma_\alpha (\mathbf{x} \cdot \mathbf{y}_\alpha) \mathbf{x} \cdot (\mathbf{y}_\alpha \times \delta s_\alpha) - \frac{1}{3} \sigma^2 \varepsilon \mathbf{x} \cdot \Omega \times \mathbf{x} \right\}, \tag{16}$$

where $\varepsilon = 4\pi \int_0^\infty \zeta(r) r^4 \, \mathrm{d}r = 3/2$ after smoothing by Equation (12) and $\Omega = \Sigma_\alpha \Gamma_\alpha \delta s_\alpha$ which is zero in unbounded inviscid flow.

3.2. COMPUTATION DETAILS

Figure 1 shows two perturbed vortex rings of unity circulation ($\Gamma = 1{\cdot}0$) at the start of simulation. The quantities with suffixes L and T denote, respectively, the initially leading and initially trailing vortex rings. The range of wavenumber is $0 \leqslant m \leqslant 5$. The ratio of vortex core radius σ to unperturbed ring radius R is chosen to be $0{\cdot}2$. Both the radial and streamwise amplitudes of the weak perturbation waves are $0{\cdot}02$ times the unperturbed ring radius and they are in-phased. The initial separation λ between the two vortices equals the unperturbed ring radius of the initially trailing vortex R_T.

During interaction, the vortex filaments suffer from vorticity stretching. The vector length σs_α increases and consequently the amount of vorticity also increases. In order to maintain the numerical resolution, the vortex vector element or vortex blob is split into two, whenever its length exceeds twice its original value [30]. Likewise, a vortex vector element or blob is fused to its nearest neighbour as its length is shorter than half of its original value. The temporal integration is effected by the fourth order Runge-Kutta scheme. All the lengths involved in the computation are normalized by the initial radius of unperturbed trailing vortex ring R_T, whereas the time t is normalized by the initial value of R_T^2/Γ_T. The accuracy of the numerical computation is monitored by the linear invariants, namely, the total vorticity and the linear vorticity impulse of potential vortex motions [29]. The allowable error is kept within one percent. The resultant vorticity impulses of the two interacting vortex rings of $1 \leqslant m \leqslant 5$ were found to be invariant with non-dimensional time $t' \leqslant 20$ [26, 28].

The divergence of the vorticity field $\nabla \cdot \boldsymbol{\omega}$ of an incompressible inviscid flow is zero. However, the discretized representation of vorticity (Equation 9) is not free of divergence for all times, even though the vortex vector elements or blobs are initially well aligned in divergence-free condition [29, 30]. Nevertheless, even after a sort duration, the vorticity representation becomes divergent as a result of discretization and numerical errors. At long time simulation significant error may occur. Several procedures have been proposed to minimize such deviation [29, 30] and Pedrizzetti's divergence filtering procedure is adopted here [30]. At each computation time step δt, the vector length δs_α is modified by,

$$\delta s_{\alpha,new} = (1 - \kappa_F) \delta s_\alpha + \kappa_F (\boldsymbol{\omega}_\alpha / |\boldsymbol{\omega}_\alpha|) \delta s_\alpha, \tag{17}$$

where $\kappa_F = \delta t / T_F$ and T_F is the filter time scale, which is adjusted between 0 to 1 with respect to the time scale of the physical phenomena. Typically, the relation $1/T_F \sim \Gamma_T / R_r^2$ holds, R_r being the radius of curvature of the vortex filaments [30].

The far field sound presssures are evaluated at a radial distance $120 R_T$ and its accuracy is monitored by means of Powell's Three-Sound-Pressure Theorem [11], which states that the sum of the pressures at equal distances on the three orthogonal axes must vanish.

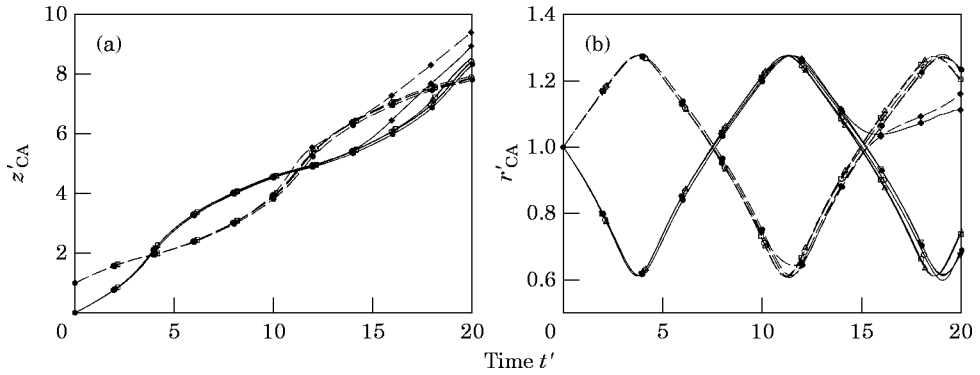

Figure 2. Streamwise positions and radii of two interacting vortex rings. (a) Streamwise positions; (b) Radii. ●, $m = 0$; ◆, $m = 1$; ○, $m = 2$; △, $m = 3$; □, $m = 4$; ▽, $m = 5$. ———, initially trailing vortex; -----, initially leading vortex.

4. RESULTS AND DISCUSSIONS

4.1. UNPERTURBED PAIRING

Interaction of two coaxial circular vortex rings propagating along their axis of symmetry in the same direction is well documented [7, 8, 12]. Under the self-induced velocity field and the induced strained field by the other vortex, the two vortices undergo the mutual slip-through or the so-called leapfrogging process. Based on the present method, by setting the perturbation amplitude to zero, the trajectories (z_{CA}, r_{CA}) of the two unperturbed interacting circular vortex rings, in the absence of swirl, are shown in Figures 2a, 2b. The accelerations of the two vortex rings are shown in Figure 3. The core to ring radius ratio σ/R is 0·2 and the initial separation λ is R_T. Unless otherwise stated, the following non-dimensional parameters are used: pressure $p' = p/(\Gamma_T/R_T)^2$ for unity density, time $t' = \Gamma_T t/R_T^2$, length $x' = x/R_T$, acceleration $\text{æ}' = \text{æ}/(\Gamma_T^2/R_T^3)$ and circulation $\Gamma' = \Gamma/\Gamma_T$. The present results agree with those of Tang and Ko [17], which was based on the vortex

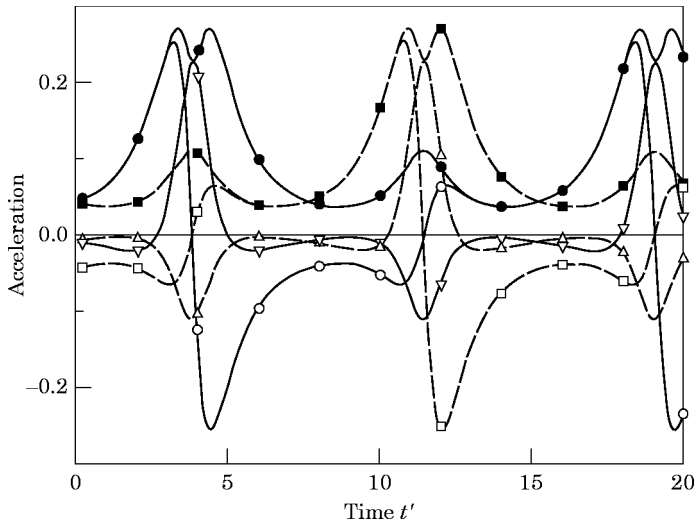

Figure 3. Accelerations of two interacting unperturbed vortex rings. $m = 0$. ■, total acceleration of initially leading vortex; ●, total acceleration of initially trailing vortex; □, streamwise component of initially leading vortex; ○, streamwise component of initially trailing vortex; △, radial component of initially leading vortex; ▽, radial component of initially trailing vortex.

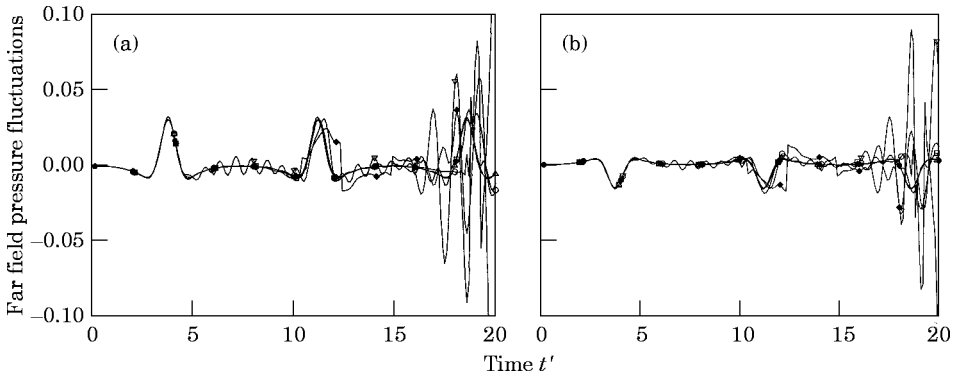

Figure 4. Maximum far field sound pressure radiated by two interacting vortex rings. (a) Major lobe; (b) Minor lobe. ●, $m = 0$; ◆, $m = 1$; ○, $m = 2$; △, $m = 3$; □, $m = 4$; ▽, $m = 5$.

filament method. Due to their mutual induction, within the time span shown in Figure 2, there are three slip throughs at the non-dimensional time t' of about 3·8, 11·4 and 18·7 (Figure 2a). Before any slip through instant, the "trailing" vortex shrinks in size and accelerates in the streamwise direction, while the "leading" one widens and decelerates (Figures 2 and 3). After the slip through instant, recovery to their original sizes occurs and their streamwise accelerations are the opposite to those before the slip through instant. The peak streamwise accelerations of the two vortex rings occur just before and after the slip through instant. However, the streamwise acceleration of the trailing vortex ring is higher than that of the leading one. Because of the changes of their sizes (Figure 2b), radial acceleration is also found for the trailing vortex ring and radial deceleration for the leading vortex during the slip through (Figure 3). As to the case of streamwise acceleration, the trailing vortex ring has higher amplitude than the leading one. For the total accelerations, the trailing vortex has much higher acceleration than the leading vortex (Figure 3).

As Equation (8) shows the far field pressure is quadrupole in nature and as will be shown later, there are significant variations in the pressure on the major (along the z-axis) and minor (normal to the z-axis) lobes, the maximum sound pressures on the two lobes occurring at the slip through instants, of the unperturbed rings are shown in Figures 4a and 4b. The results agree well with the predicted pairing sound [15, 17]. The sound pressure is dominated by the contributions from the radial acceleration of the trailing vortex (Figure 3), indicating the strong coupling between the far field sound pressure and the acceleration of the interacting vortex rings [17].

The isocontours of the instantaneous far field pressure at a radius of $120R_T$ at the first slip through instant $t' = 3{\cdot}8$ are shown in Figure 5. The values of the three axes represent the non-dimensional pressure p'. As the isocontours of the outer two slip throughs are the same, they are not presented. The isocontours indicate the quadrupole characteristics with the pressure on the major lobe being bigger than that on the minor lobe.

4.2. PERTURBED PAIRING

For $m = 1$ the two interacting vortex rings at different time t' are shown in Figures 6a–6d. At $t' = 0$ the two rings are tilted in the same direction on the xz-plane (Figure 6a). At $t' = 3{\cdot}6$, the tilted initially trailing ring, now only having about 60% of its original diameter, is slipping through the nearly un-tilted initially leading ring, the diameter of which increases by about 30% (Figure 6b). The time of the first slip through instant at $t' \approx 3{\cdot}7$ of $m = 1$ agrees with that of unperturbed rings. At the second slip through instant $t' \approx 11{\cdot}4$, the main differences from the first slip through and from the unperturbed case

are, besides changing their roles, that the two rings are eccentric and their tilts are, in opposite direction (Figure 6c). Although they are eccentric, their shapes are still basically circular. Because of the tilted conditions, the time required for the complete slip through is $\Delta t' \approx 1{\cdot}1$. Later at $t' = 17$, the two rings develop, especially the initially trailing one (the trailing one), into shapes significantly different from their original (Figure 6d). Even at $t' = 20$, the trailing vortex still has not slipped through the leading one (not shown here).

The axial positions z'_{CA} and radii r'_{CA}, based on Equation (5), of the two perturbed vortex rings at $m = 1$ are also shown in Figures 2a and 2b. The results of the first slip through agree with those of unperturbed rings. Before and at the second slip through, there is only slight difference in the results. After the second slip through instant $t' \approx 11{\cdot}4$, significant differences in the z'_{CA} and r'_{CA} indicate that the global shapes of the rings also do not indicate clear third slip through.

Based on the maximum peak to peak streamwise and radial perturbation amplitudes, the normalized growth rates $(R_T/\Gamma_T)\,\mathrm{d}\Delta z/\mathrm{d}t$ and $(R_T/\Gamma_T)\,\mathrm{d}\Delta r/\mathrm{d}t$ of the two vortices are shown in Figures 7a and 7b. There is progressive increase in the growth rates of the two vortices after each slip through with the streamwise growth rates of the two vortices being higher than the radial ones during the last two slip throughs.

The normalized streamwise, radial and total accelerations of the two perturbed vortex rings at this $m = 1$ are shown in Figure 8. During the first slip through, both the streamwise and radial accelerations of this perturbed case are the same as those of unperturbed rings (Figure 3). During the second slip through, the total acceleration is more than double that of the first slip through and is mainly due to the contribution from the streamwise component of the trailing vortex (initially leading vortex), which also has lower radial acceleration than that of the first slip through. It is different from the first slip through

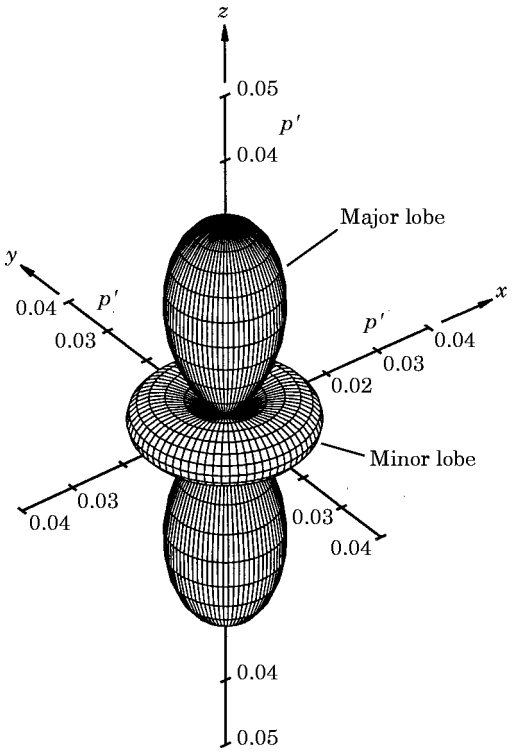

Figure 5. Isocontours of far field sound pressure at slip through instant. $m = 0$. $t' = 3{\cdot}8$.

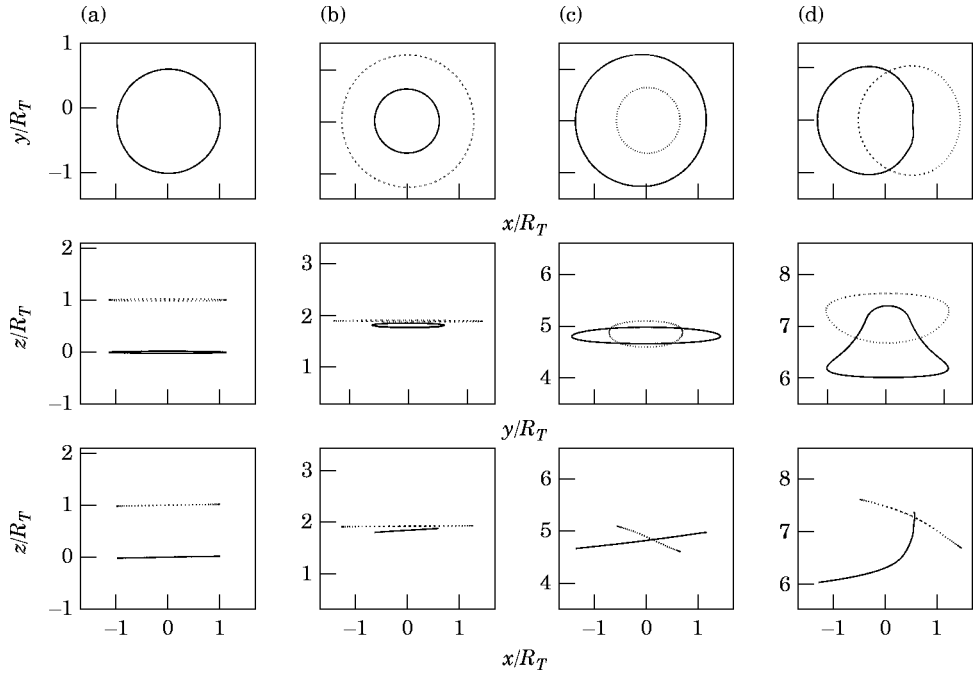

Figure 6. Interaction of two perturbed vortex rings. $m = 1$. (a) $t' = 0$; (b) $t' = 3{\cdot}6$; (c) $t' = 11{\cdot}4$; (d) $t' = 17$. ———, initially trailing vortex; ·····, initially leading vortex.

in that contributions from both components are as significant. After the second slip through instant, the accelerations are significantly different from those of the other two slip throughs in that no dominant peak is found. This may be due to the absence of clear slip through (Figures 2a and 6d).

The maximum sound pressures on the major and minor lobes at $m = 1$ are also shown in Figure 4. Due to the contamination of high frequency error during computation, all the pressure distributions were low pass filtered [31]. As expected, the pressures during the first slip through are the same as those of the unperturbed cases. Although the peak pressures of the second slip through are nearly the same as those of the first slip through and of the unperturbed case, the shapes of the pressure peak seem to be different and wider. This may be due to the longer slip through and different slip through pattern as discussed above (Figure 6c). For the third slip through, the pressures on both lobes are significantly higher and of higher frequency.

For this wavenumber $m = 1$, there is still coupling between the sound pressure and acceleration during the first and second slip throughs (Figures 4 and 8). During the third slip through, coupling between the pressure and acceleration is still found, even though they are of higher frequency. This means that the average or global streamwise position z_{CA} and radius r_{CA} and their time derivatives still confirm the relationship between the accelerations of the vortex rings and the far field sound pressure.

The isocontours of the instantaneous sound pressure p' at $t' = 11{\cdot}8$ and $18{\cdot}5$ at the second and third slip through instants are shown in Figures 9a and 9b. As the isocontours at the first slip through instant are the same as those of the unperturbed case, they are not shown here. The isocontours indicate, though still quadrupole in nature, the principal axes are rotated and the pressures of both lobes are nearly of the same magnitude. The isocontours at other times, not shown here, indicate the rotation of the principal axes

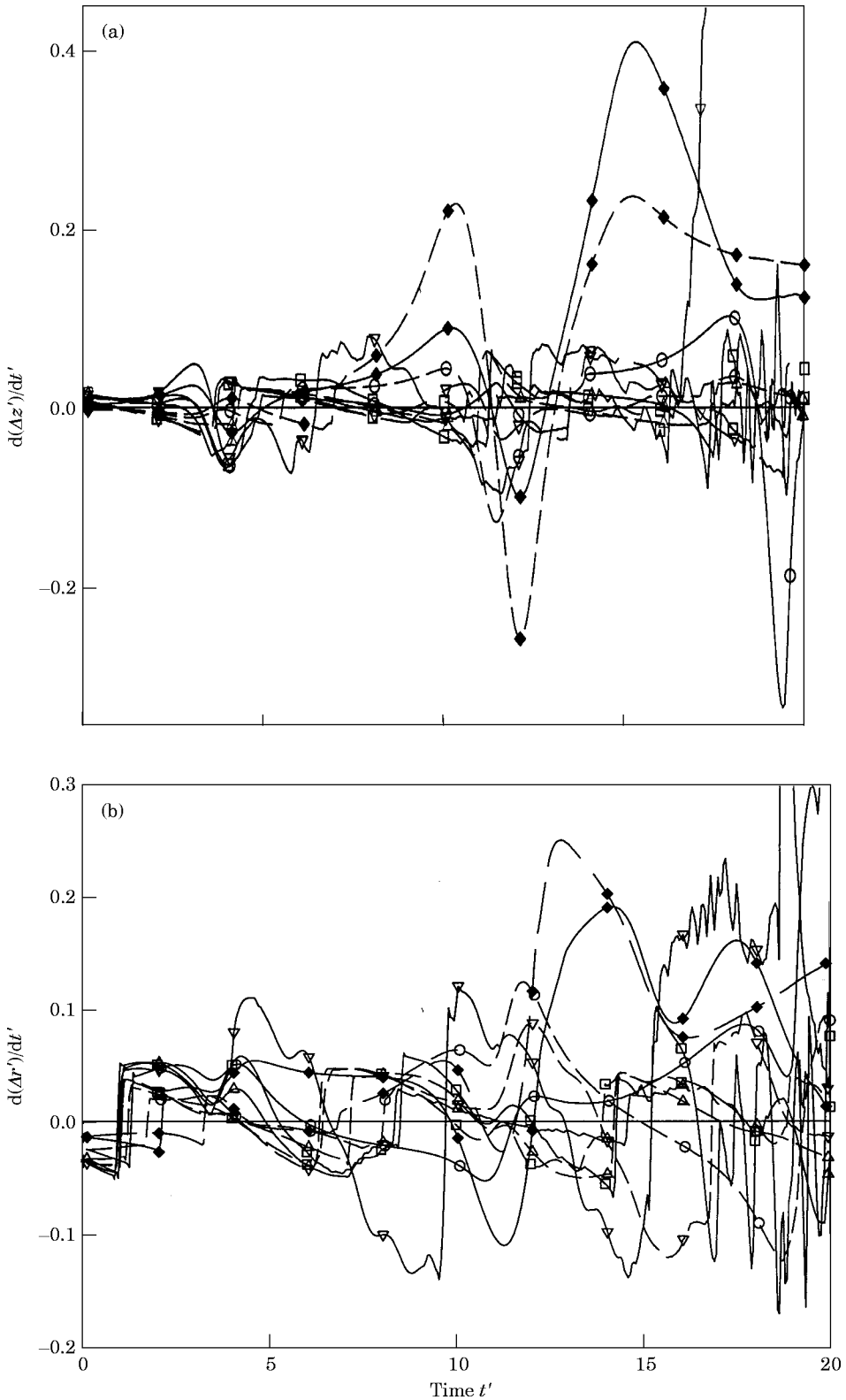

Figure 7. Growth rates of two perturbed vortex rings. (a) Streamwise; (b) Radial. ◆, $m = 1$; ○, $m = 2$; △, $m = 3$; □, $m = 4$; ▽, $m = 5$. ———, initially trailing vortex; -----, initially leading vortex.

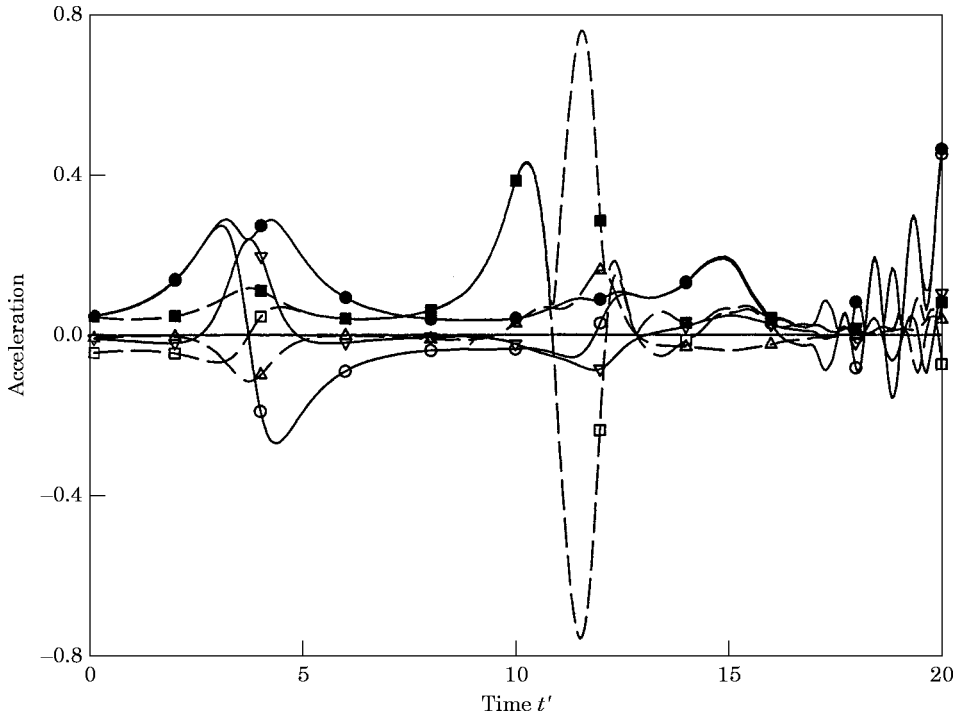

Figure 8. Accelerations of two interacting vortex rings. $m = 1$. ■, total acceleration of initially leading vortex; ●, total acceleration of initially trailing vortex; □, streamwise component of initially leading vortex; ○, streamwise component of initially trailing vortex; △, radial component of initially leading vortex; ▽, radial component of initially trailing vortex.

during the interaction of the two vortex rings. This rotation of the principal axes of the quadrupole is different from the stationary one of the unperturbed case (Figure 5).

For $m = 2$ Figures 10a to 10d indicate the change of shape, circular or elliptical, and of size, bigger or smaller, of the two interacting perturbed vortex rings. During the third slip through, the two rings are elliptical and perpendicular to each other (Figure 10d).

In the study of the evolution of a plane elliptic vortex ring of thin core ($m = 2$) of Dhanak and Bernardinis [32], for the initial axis ratio close to 1, the vortex ring oscillates periodically. This suggests that by themselves, the two present elliptic vortex rings of initial axis ratio very close to 1 may also be under their own self oscillations, besides the induced field due to the other vortex. For the case of initial axes ratio $b/a = 0{\cdot}8$, where a and b are the major and minor axes, Dhanak and Bernardinis [32] show that the elliptic vortex changes from a flat shape in the beginning to one with curvature and back to a flat shape at half period. At half period it is also elliptical in shape with the orientation of its axis reversed and the axis ratio b/a is also 0·8, the same as that initially. For the present case of $m = 2$, the perturbed initially trailing vortex has an initial axis ratio b/a of 0·96 and it develops into a flat elliptic vortex at $t' = 4{\cdot}8$ with an axis ratio of 0·8, after the first slip through. This ratio of 0·8 and its flatness are nearly maintained over the period $4{\cdot}5 \leqslant t' \leqslant 5{\cdot}0$ (results not shown). Then, it develops and has a ratio b/a of 0·98 at the second slip through instant of $t' = 11{\cdot}2$ (Figure 10c). Further downstream, this trailing vortex develops into a shape, not exactly elliptical, with more flatness on the minor side at $t' = 16$ (not shown). This particular shape is similar to that of the evolving elliptic vortex ring of axis ratio of 0·4 [32].

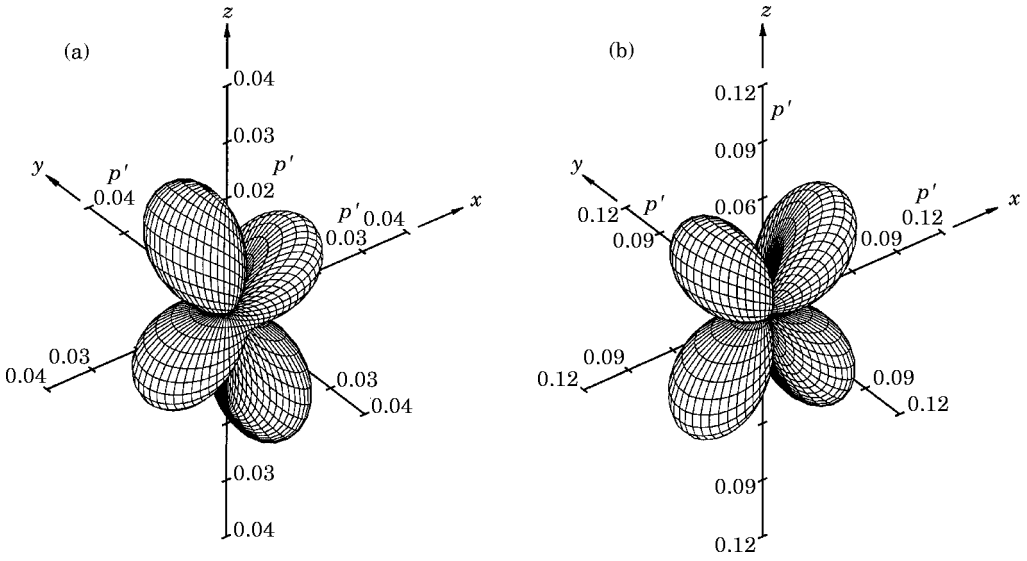

Figure 9. Isocontours of far field sound pressure at second and third slip through instants. $m = 1$. (a) $t' = 11{\cdot}8$; (b) $t' = 18{\cdot}5$.

The above comparison of the development of the initially trailing vortex with that of a single elliptic vortex [32] suggests that because of its initial axis ratio being very close to 1, its development before, during and soon after the first and second slip throughs of $t' < 12$ follows that of a single elliptic vortex. Further development of the present initially trailing vortex seems to follow more of that of axis ratio 0·4 [32]. It would further suggest

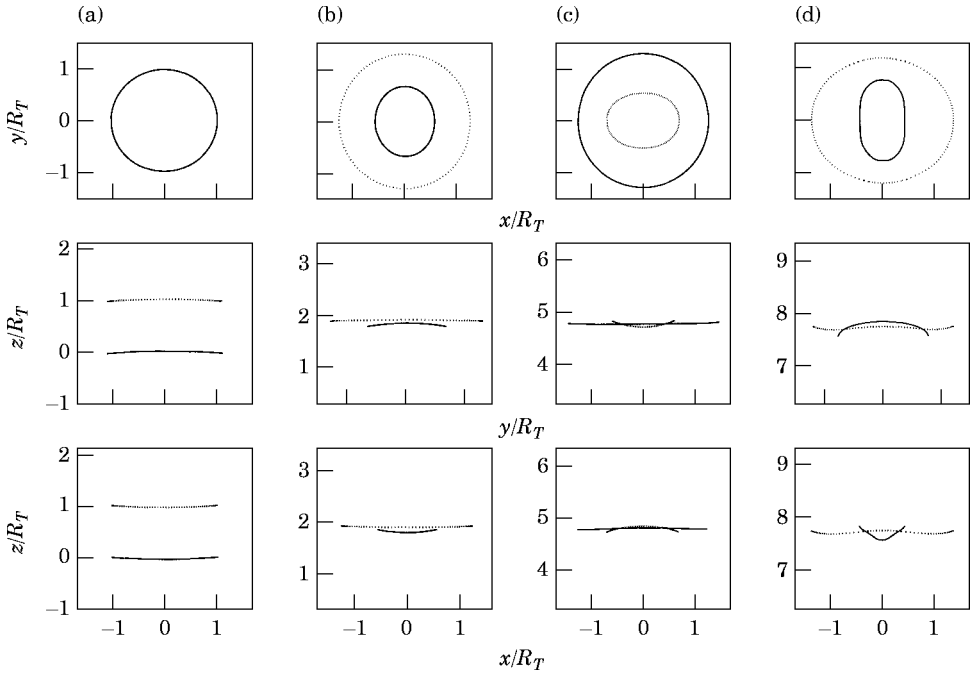

Figure 10. Interaction of two perturbed vortex rings. $m = 2$. (a) $t' = 0$; (b) $t' = 3{\cdot}6$; (c) $t' = 11{\cdot}2$; (d) $t' = 19$.

that for the first and second slip throughs, interaction of the present weakly perturbed vortex rings does not significantly affect the development of the initial trailing vortex. It is only after the second slip through that interaction significantly affects its evolution and its behaviour seems to be that of a lower axis ratio.

For the present initially leading vortex $m = 2$ the axis ratio b/a increases from 0·96 at $t' = 0$ to 1·0 at $t' = 1{\cdot}5$ and decreases to its initial value 0·96 at $t' = 4{\cdot}2$, after the first slip through. At this time, the vortex is nearly flat. At $t' = 8$, $b/a = 1$ again. Later, the axis ratio decreases to 0·67 at $t' = 14$, after the second slip through. It increases to 0·89 at $t' = 19$ of the third slip through. This behaviour of the present initially leading vortex suggests that its near circular shape at $t' < 8$ indicates much smaller oscillation during and after the first slip through. At $t' > 8$ its oscillation is bigger with $b/a = 0{\cdot}67$ at $t' = 14$, before it increases again. The above indicates that the initially leading vortex behaves differently from the initially trailing vortex in that the amplitude of oscillation of the former is smaller than that of the latter, even though their initial conditions are the same. This different effect of interaction on the evolution of the two vortices may be due to the higher acceleration, both streamwise and radial, and its stabilization on the trailing vortex during the first slip through. At the second slip through, the bigger oscillation of the initially leading vortex to $b/a = 0{\cdot}67$ and its different behaviour from the evolving single elliptic vortex may be due to the more significant mutual induction and strain on the two interacting vortices, resulting in bigger curvature or azimuthal component of the initially leading vortex (Figures 10b to 10c).

For this wavenumber of 2 the normalized streamwise and radial growth rates are also shown in Figures 7a and 7b. Of the first slip through, the growth rates of both vortices are of the same order of magnitude as those of $m = 1$. For the second and third slip throughs, both growth rates of this wavenumber are generally lower than those of $m = 1$.

The normalized streamwise, radial and total accelerations of the two perturbed vortex rings at $m = 2$ are shown in Figure 11. The accelerations of the vortices of the first two slip throughs are the same, agreeing with those of the unperturbed case (Figure 3). Compared with $m = 1$, the accelerations during the first slip through are the same, while those during the second slip through are different (Figure 8). The accelerations during the third slip through at $t' \approx 19$ are generally higher, though a similar pattern to those of the first and second slip throughs is found.

The maximum sound pressures on the major and minor lobes at $m = 2$ are shown in Figure 4. The peak pressures of the second slip through are slightly higher than those of the first slip through. For the third slip through, the peak pressures on both lobes are slightly higher than those of the second slip through. However, the distributions of the three slip throughs are basically the same, similar to those of $m = 0$ and significantly different from the third slip through of $m = 1$.

The isocontours of the sound pressure p' of the two perturbed vortex rings of $m = 2$ during the second and third slip throughs are shown in Figures 12a to 12d. As the distribution at the first slip through instant $t' = 3{\cdot}8$ of this wavenumber is the same as that of $m = 1$ and of the unperturbed case, it is not shown here. For the second slip through, at the slip through instant $t' = 11{\cdot}2$, the sound pressures are the highest and the distribution is also basically quadrupole in nature (Figure 12a). However, the minor lobe (on the xy-plane) is bisymmetric, even though it is still parallel to the xy-plane and without any tilt. The sound pressures on both lobes at this instant of the second slip through are slightly higher than those of the first slip through, suggesting that the effect of perturbation becomes significant during the second slip through. Just after the slip through instant at $t' = 11{\cdot}4$, the distribution has lower pressures and is again of quadrupole nature and the bisymmetry of the minor lobe disappears (Figure 12b). This

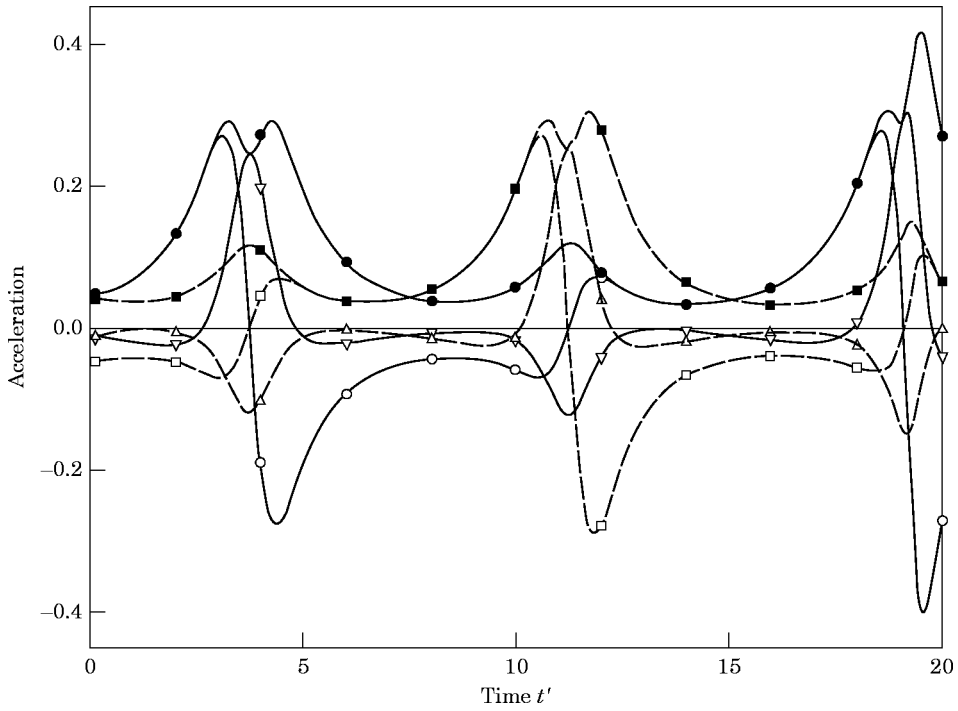

Figure 11. Accelerations of two interacting vortex rings. $m = 2$. ■, total acceleration of initially leading vortex; ●, total acceleration of initially trailing vortex; □, streamwise component of initially leading vortex; ○, streamwise component of initially trailing vortex; △, radial component of initially leading vortex; ▽, radial component of initially trailing vortex.

rapid change of sound pressure and its directivity characteristic are associated with similar rapid change of the acceleration (Figure 11). This illustrates the difficulty encountered in measuring the time dependent sound field and its instantaneous directivity [33]. During the third slip through $t' = 19$, although it is still quadrupole in nature, the pressure on the xy-plane is higher (Figure 12c). This switching of the major and minor axes is also reported during the evolution of a single elliptic vortex ring [32]. Further, the maximum sound pressures of the two lobes are higher than the corresponding ones of the second slip through, suggesting that the effect of perturbation becomes more significant with further interaction of the two vortices.

In the study of Michalke and Fuchs [34] the azimuthal instabilities of the first two azimuthal modes $m = \pm 1$ and ± 2 are unstable and grow within the first few diameters of the jet. In the present study, for $m = 1$ the initially trailing vortex starts its interaction with a tilt of $\phi_T \approx 1{\cdot}7^\circ$ (Figure 6a). At $t' = 3{\cdot}6$, just before the first slip through, $\phi_T \approx 2{\cdot}4^\circ$ (Figure 6b). At $t' = 11{\cdot}4$, during the second slip through its tilt angle (leading vortex) increases to $\phi_T \approx 6{\cdot}5^\circ$. For the initially leading vortex, however, it starts with $\phi_L \approx 1{\cdot}7^\circ$, reduces very slowly to $\phi_L \approx 0{\cdot}9^\circ$ just before the first slip through at $t' = 3{\cdot}6$ and at $t' = 6{\cdot}5$, $\phi_L \approx 0^\circ$. Further downstream, its tilt angle (trailing vortex) increases fairly rapidly to $\phi_L \approx -21{\cdot}5^\circ$ at $t' = 114$, during the second slip through. At $t' = 13$, its tilt angle decreases rapidly to $\phi_L \approx -8{\cdot}7^\circ$. As the two slip throughs occur within the first six initial radii of the vortex rings, the growth of the azimuthal instabilites of the two rings depends on whether they act as the leading and trailing vortex (Figure 7). As presented above, for $m = 1$, the growth of the trailing vortex (initially leading vortex) involves a tilt from $\phi_L \approx -21{\cdot}5^\circ$ at $t' = 11{\cdot}4$ during the second slip through to $\phi_L \approx -8{\cdot}7^\circ$ at $t' = 13$, at which

time the radial growth rate is highest (Figure 7b). As the two vortices still nearly maintain their circular shapes, the eccentricity, distortion and opposite phase of their tilts during their interaction may be responsible for the significant growth of the initially leading vortex. Further discussion will be presented later.

Physically, the presence of the $m = \pm 1$ helical modes indicates the tilts of the interacting vortex rings [33]. The presence of the bisymmetric $m = \pm 2$ modes represents the deformation of a circular ring into an elliptic ring. Thus, the results of the present study of $m = 2$ show that the deformation of the nearly circular rings into elliptic rings during

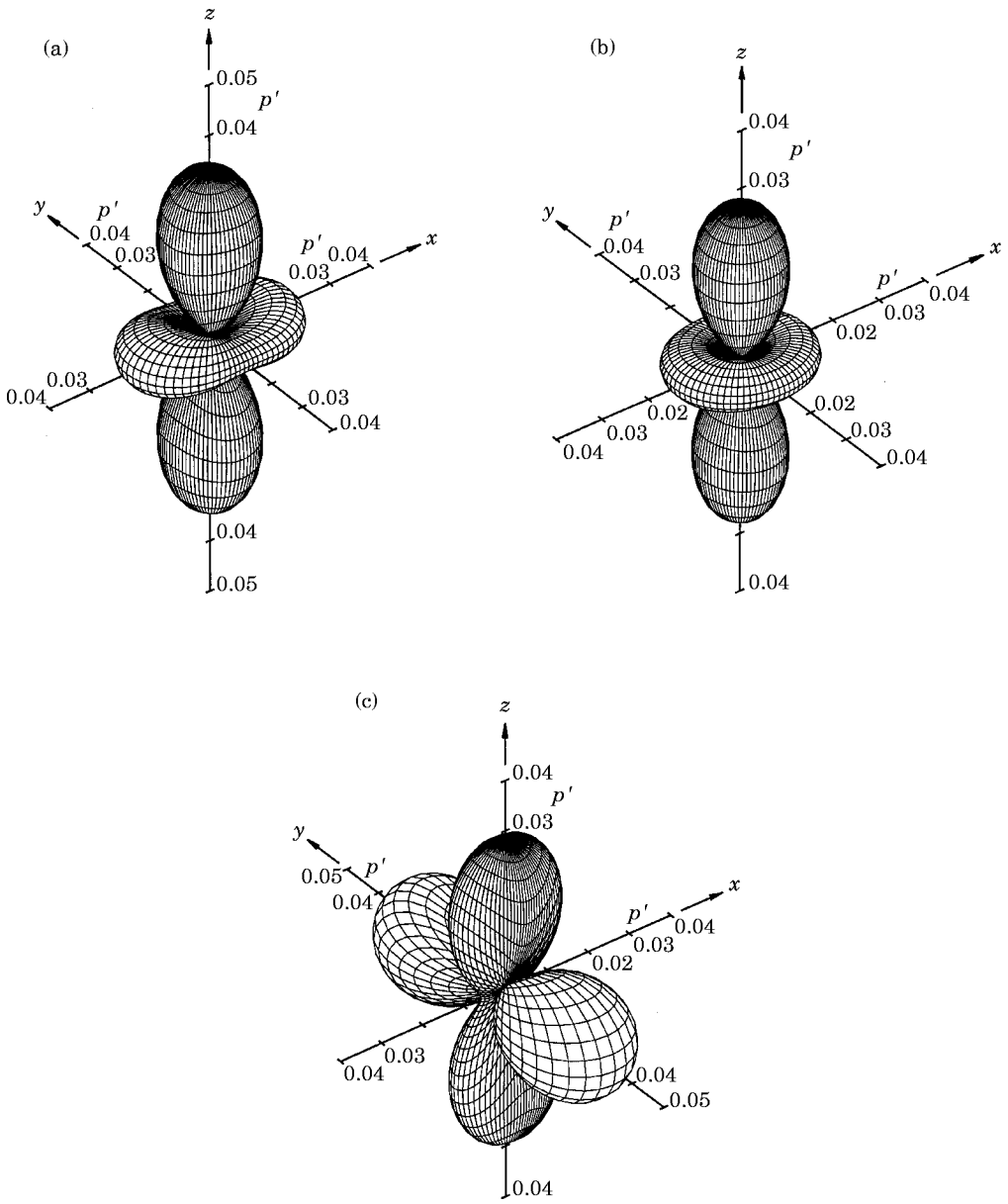

Figure 12. Isocontours of far field sound pressure during second and third slip throughs. $m = 2$. (a) $t' = 11{\cdot}2$; (b) $t' = 11{\cdot}4$; (c) $t' = 19$.

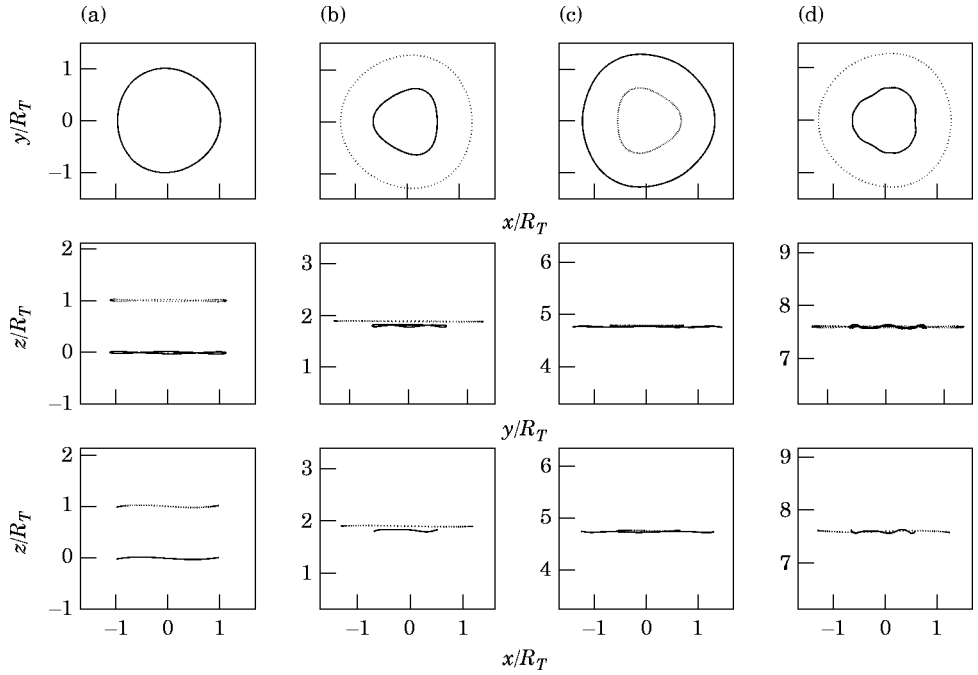

Figure 13. Interaction of two perturbed vortex rings. (a) $t' = 0$; (b) $t' = 3{\cdot}6$; (c) $t' = 11{\cdot}2$; (d) $t' = 18{\cdot}6$. ———, initially trailing vortex; ·····, initially leading vortex.

their interaction is the same as those of unperturbed vortex rings, indicating that the deformation of the initially trailing vortex into elliptic one does not generate "extra" sound during the first slip through. The bisymmetric deformation during the second slip through involves more sound radiated. During the third slip through, the interaction of two normally orientated elliptic rings results in higher sound radiated and change in its directivity. The higher sound generated of $m = 1$ during the third slip through may be the cause for the experimental observation, based on statistical approach, of Michalke and Fuchs [34] that the first azimuthal mode $m = 1$ dominates the second mode $m = 2$ by a factor of 3:1. However, the present findings do not seem to agree with the statistical experimental findings of higher contribution of the axisymmetrical mode than that of the first mode by a factor of 1·3:1 of Michalke and Fuchs [34] and 16:1 of Ghosh *et al*. [33]. This significant difference in the experimental results of the above workers may be due to the difference in the initial conditions of the nozzles whether there are any inherited azimuthal disturbances or not.

For $m = 3$ the perturbed rings at $t' = 0$ and at the three slip through instants are shown in Figures 13a to 13d. Basically, for the first and second slip throughs the vortices still maintain their basic forms and are in-phased (Figures 13a to 13c). At the third slip through, higher wavenumber waves are found (Figure 13d). Even during the third slip through, the two vortices are nearly planar and parallel to each other, without any tilt.

In the study of a water jet by Paschereit *et al*. [22], under axisymmetric forcing the initial laminar vortices seem to have a wavenumber of 3. The patterns of the vortices during interaction and slip through and their higher wavenumber waves further downstream are very similar to those of the second and third slip through of $m = 3$ of the present study (Figures 13c and 13d).

The streamwise and radial growth rates of this wavenumber are nearly the same for the three slip throughs (Figures 7a to 7b). As the accelerations of the two vortices of this wavenumber are nearly the same for the three slip throughs and are the same as those of the unperturbed case (Figure 3), they are not presented. The maximum sound pressures on the major and minor lobes, are shown in Figure 4, are the same as those of the unperturbed case. The isocontours of the sound pressure near the slip throughs of this $m = 3$, not shown here, are basically the same as those of the unperturbed case and there is no rotation of the directivity.

For this wavenumber $m = 3$ the above results indicate the same characteristics as those of unperturbed vortices, indicating that perturbation has no significant effect on their interaction and on the far field sound radiated.

For $m = 4$ the perturbed rings at $t' = 0$ and at the three slip through instants are shown in Figures 14a to 14d. For the first and second slip throughs, the vortices still maintain their basic waveforms (Figures 14a to 14c). During the third slip through, the initially leading vortex has eight waves, while the initially trailing vortes has more than eight, even though they are still mainly in-phased. During the interaction, the two vortices are nearly planar and parallel to each other, without any tilt.

The streamwise and radial growth rates of this wavenumber are significantly different at the third slip through (Figure 7), at which high frequency components are found. This deviates from those of other wavenumbers $1 \leqslant m \leqslant 3$ presented above. These growth rates are lower than those of $m = 1$, but significantly higher than those of $m = 2$ and 3.

As the accelerations of the three slip throughs are the same as the unperturbed case, they are not presented. The maximum sound pressures on the major and minor lobes of this wavenumber $m = 4$ are shown in Figures 4a and 4b. The peak pressures of the first and second slip throughs are the same as those of the unperturbed case. Those of the third

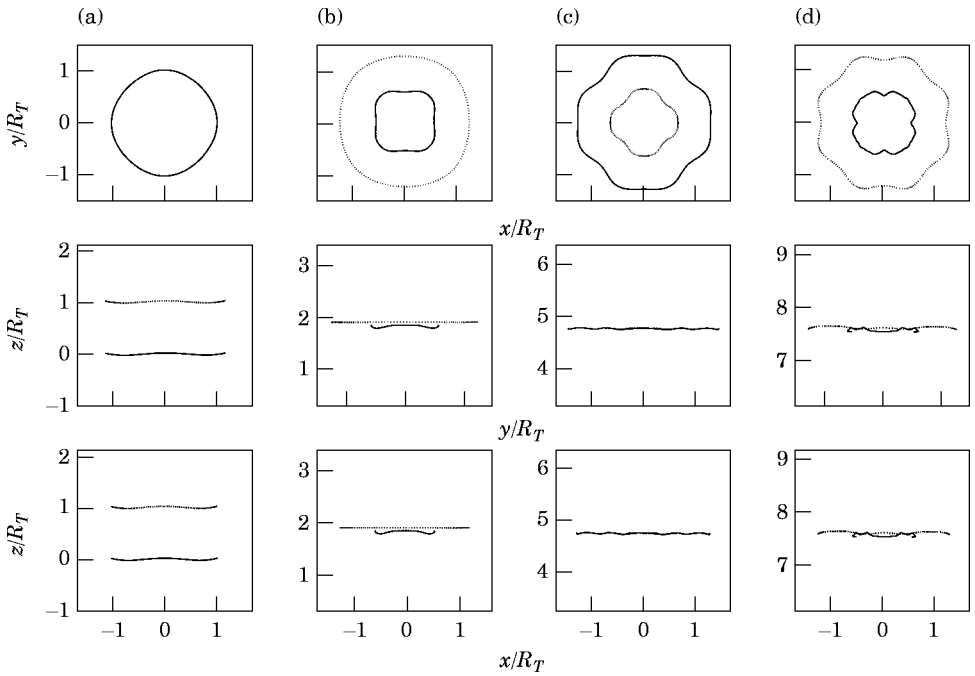

Figure 14. Interaction of two perturbed vortex rings. $m = 4$. (a) $t' = 0$; (b) $t' = 3{\cdot}6$; (c) $t' = 11{\cdot}2$; (d) $t' = 18{\cdot}6$. ———, initially trailing vortex; ·····, initially leading vortex.

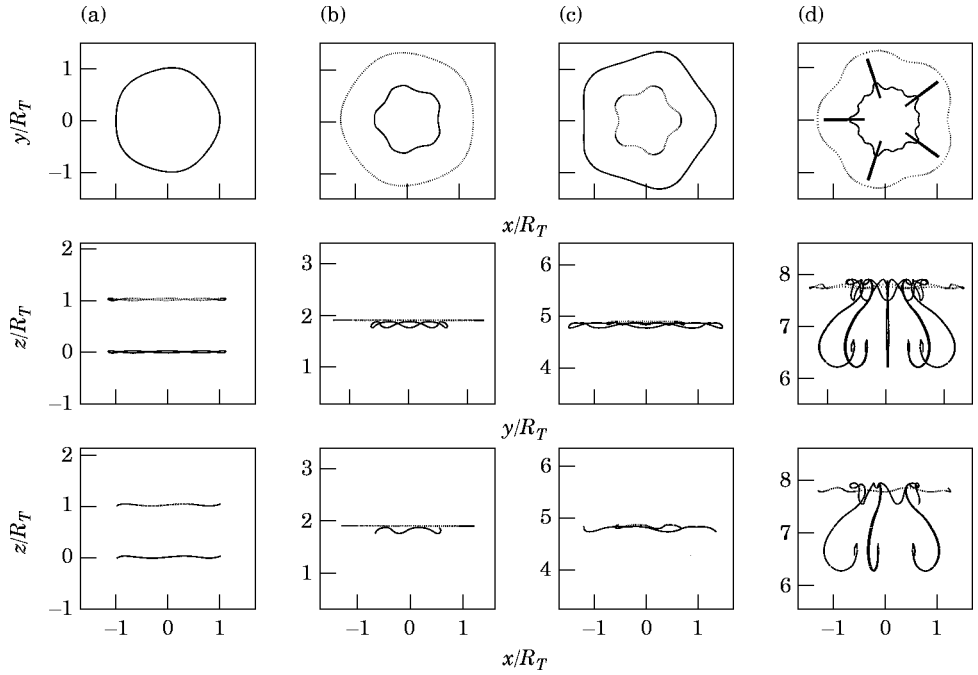

Figure 15. Interaction of two perturbed vortex rings. $m = 5$. (a) $t' = 0$; (b) $t' = 3{\cdot}6$; (c) $t' = 11{\cdot}4$; (d) $t' = 19$. ———, initially trailing vortex; ·····, initially leading vortex.

slip through are slightly higher. There are smaller peaks of high frequency at $16 < t' < 18$, during which both vortices have waves double or more than its original wavenumber of 4 (Figure 14d), suggesting local induction or stretching of these smaller vortical structures. The local interaction of these smaller structures may not be shown by the global acceleration of this wavenumber.

Although the sound pressures near the third slip through instant $t' = 18{\cdot}6$ are higher than those of the first and second slip throughs of this wavenumber and of the unperturbed case, the shape of the isocontours and directivity, however, are still the same with no rotation of their axes (not shown here).

For $m = 5$ the perturbed rings at $t' = 0$ and at the three slip through instants are shown in Figures 15a to 15d. For the first and second slip throughs, the basic forms are still maintained (Figures 15a to 15c). For the third slip through, however, dramatic changes in the initially trailing vortex (trailing vortex) is found (Figures 15d). The initially trailing vortex becomes a star-like structure with long "tails" trailing behind the ring. The ring itself has higher frequency waves and the streamwise amplitudes of the waves are much higher than those of the initially leading vortex.

In the study of laminar co-flowing jet of Lasheras *et al*. [35], for the number of lobes in the corrugated nozzle of 5 ($m = 5$), the small amplitude streamwise forcing resulted in two interacting perturbed rings. The horizontal cross-cut of the jet at a downstream distance of three jet diameters indicates the two vortices of $m = 5$ and they are in-phased. It is at this position that the instability of the vortex ring is still fairly stable and the amplitude has not grown appreciably [33]. They are of the same patterns as those of the present study, as shown in Figure 15c, during the second slip through $t' = 11{\cdot}4$ and at about 2·5 ring diameters downstream. Also shown in Figure 15c, the vortices have not

grown appreciably, suggesting that the amplification of the ring stability is not yet high (Figures 15a to 15b).

In the study of a water jet by Paschereit *et al*. [22], under axisymmetrical forcing at two frequencies, the streakline patterns of the two laminar vortices have waves on the rings just before and after the slip through. Although the wavenumbers of the two vortices were not estabilished, the trailing vortex, soon after the slip through instant, has long "tails" or sheath of vortical material trailing behind the ring. It is very similar to the pattern of the initially trailing vortex (trailing vortex) during the third slip through $m = 5$ (Figure 15d).

In the study of a forced water jet by Browand and Laufer [36], the two interacting vortex rings have perturbations of wavenumber $m = 5$. During the slip through, large streamwise amplitude of the inner trailing vortex is observed. After the slip through of the remainder of the trailing vortex core, sheath of vortical materials is still in the process of slipping through the outer leading ring. These phenomena are also very similar to those of the third slip through (Figure 15d).

The above agreement of the flow visualization observation of the sheath of vortical material with those of the third slip through of the present study is also indicated by the large streamwise growth rate at this slip through (Figure 7a). The streamwise growth rate of this wavenumber $m = 5$ is significantly higher than that of the corresponding slip through of other wavenumbers (Figure 7a). This indicates the dramatic effect of interaction of the two vortices at this wavenumber. Further discussion will be presented later.

The accelerations of the two vortices at this wavenumber $m = 5$ are shown in Figure 16. For the streamwise acceleration, high frequency components of the initially trailing vortex (trailing vortex) are found during the third slip through. The large streamwise

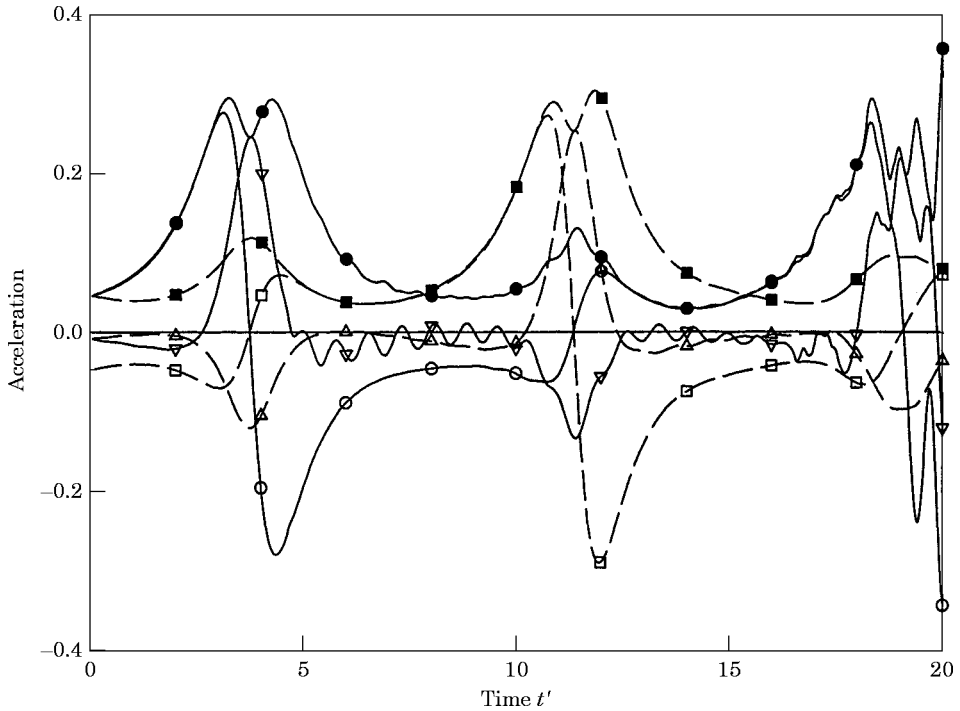

Figure 16. Accelerations of two interacting vortex rings. $m = 5$. ■, total acceleration of initially leading vortex; ●, total acceleration of initially trailing vortex; □, streamwise component of initially leading vortex; ○, streamwise component of initially trailing vortex; △, radial component of initially leading vortex; ▽, radial component of initially trailing vortex.

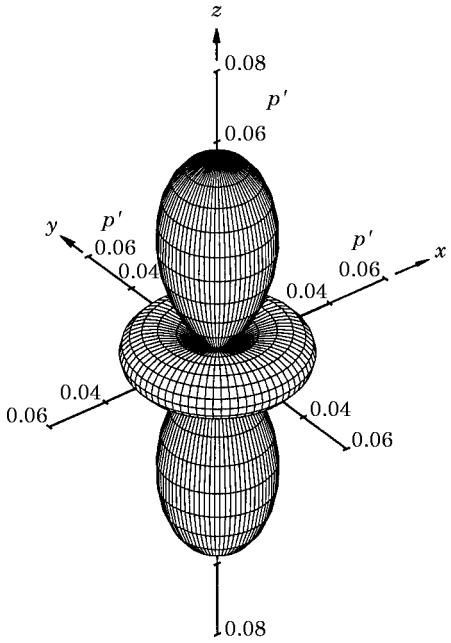

Figure 17. Isocontours of far field sound pressure at third slip through instant. $m = 5$. $t' = 18{\cdot}0$.

growth rate and the long "tail" of the initially trailing vortex during this slip through do not significantly affect the global streamwise acceleration. Rather, they affect the radial acceleration and total acceleration with bigger amplitude high frequency components during the third slip through (Figure 16). At this wavenumber, there are also high frequency components of the radial acceleration between the first and second slip throughs (Figure 16). This results in the presence of high frequency components of the maximum sound pressures of the major and minor lobes (Figures 4a and 4b). For the third slip through, the pressures are of high frequency and are much higher than those of the first slip through and of the unperturbed case. The above findings indicate a certain amount of coupling between the high frequency components of the global radial acceleration with the sound radiated.

The isocontours of the sound pressure of this wavenumber at the third slip through instant $t' = 18$ are shown in Figure 17. The isocontours indicate higher pressure on both lobes. At the first and second slip through instants, they are basically the same and are the same as those of the unperturbed case. However, the directivity of the sound is the same as the other two slip throughs and as the unperturbed case. There is also no rotation of the principal axes of the quadrupole.

5. REMARKS

The above sections present the interaction of two slightly perturbed thin vortex rings of wavenumbers $1 \leqslant m \leqslant 5$. As the interaction is very complicated, the following tries to explain in more detail the important findings and comparison with a single vortex ring. For a single thin vortex ring, for wavenumbers smaller than that of the unstable mode m^*, the radial perturbation produces a streamwise perturbation almost of the same amplitude [23]. They are linearly stable since their amplitudes remain bounded and their time variations are periodic. At the unstable wavenumber m^* the amplitude of perturbation

increases exponentially. Widnall and Sullivan [19] suggest that a mode becomes unstable when the self induced rotation of the wave balances the rotation induced by the ring and the energy of the perturbation is expended in stretching the wave amplitude.

The estimated unstable mode of a single vortex of the present parameters, not shown here, is $m^* = 8$. This wavenumber agrees with $m^* = 7$ of Widnall and Sullivan [19] and with $m^* = 8$ of Knio and Ghoniem [23]. Thus, the individual vortices, by themselves, of $1 \leqslant m \leqslant 5$ of the present study are within the linearly stable regime. In this regime the growth and amplitudes (peak to peak) in both streamwise and radial directions of each individual vortex under the present perturbation are also stable and antiphased (only the results normalized by the initial perturbation of $m = 2$ and 5 are shown in Figures 18a and 18b), basically agreeing with those of Knio and Ghoniem [23].

For a single vortex ring and core to ring radius ratio of 0·25, Knio and Ghoniem [23] found that the unstable mode occurs at $m^* = 6$. The shape of the single vortex ring at $t' = 210$, near its final stage of evolution, is very similar to the evolution of the initially trailing vortex of $m = 5$ of the present study of two interacting perturbed vortex rings during the third slip through at $t' = 18$ (not shown here) and also similar to the more developed form $t' = 19$ (Figure 15d). The linear stage, the non-linear stage and the violent stretching of the hairpin vortices [23], are also found during their interaction and evolution (Figure 15). During the third slip through, the fold backwards and highly stretched hairpin vortices towards the original axis of the ring are responsible for the ''tails'' shown in Figure 15d. However, in the present study, the ''tails'' or fold backwards hairpin vortices are much more highly stretched than those of the single vortex [23]. This difference may be due to the presence of the other vortex (outer initially leading vortex) and its induction, besides the self induction, on the trailing vortex (initially trailing vortex), which is undergoing acceleration and shrinkage. This results in different movement, velocities and accelerations of different parts of the deformed core. As presented above, these ''tails'' or much elongated hairpin vortex structures of the present $m = 5$ of two interacting perturbed vortex rings are confirmed by the results of flow visualization [1, 9, 22, 36]. The above behaviour of the present interacting trailing vortex (the initially trailing vortex) of $m = 5$ during the third slip through corresponds to the unstable mode of a single vortex $m^* = 7$. This means that because of interaction, this interacting vortex has its unstable mode reduced from $m^* = 8$ to $m^* = 5$.

The evolution of the two interacting vortices of the present $m = 5$ also shows different behaviour (Figure 15). At the first slip through instant $t' = 3{\cdot}6$ (Figure 15b), though the initially trailing vortex has the tendency to develop the five lobes or hairpin vortices, it does not evolve into an unstable one during its role changes to the outer leading vortex of the second slip through (Figure 15c). Similarly, during the second slip through the inner trailing vortex (initially leading vortex) also does not evolve into an unstable one (Figures 15c and 15d). During these two slip throughs, the accelerating and shrinking trailing vortex experiences an increase in its radial amplitude and the leading vortex either has much smaller increase or even decrease in its radial amplitude (Figure 18b). This difference between the evolution of the trailing vortex of the first two slip throughs with that of the third slip through may be due to the more rapid streamwise growth of the initially trailing vortex, even during the first slip through (Figures 15b to 15d and 18a). This suggestes that there may be a critical streamwise amplitude of the trailing vortex, beyond which the vortex grows exponentially, as of the unstable mode.

For single perturbed vortex ring, Knio and Ghoniem [23] found that for linearly and neutrally stable modes the maximum amplitude (normalized by the initial perturbation) of the vortex during its evolution is equal to or less than unity in the streamwise and radial directions. At the unstable mode the streamwise amplitude reaches unity, soon after the

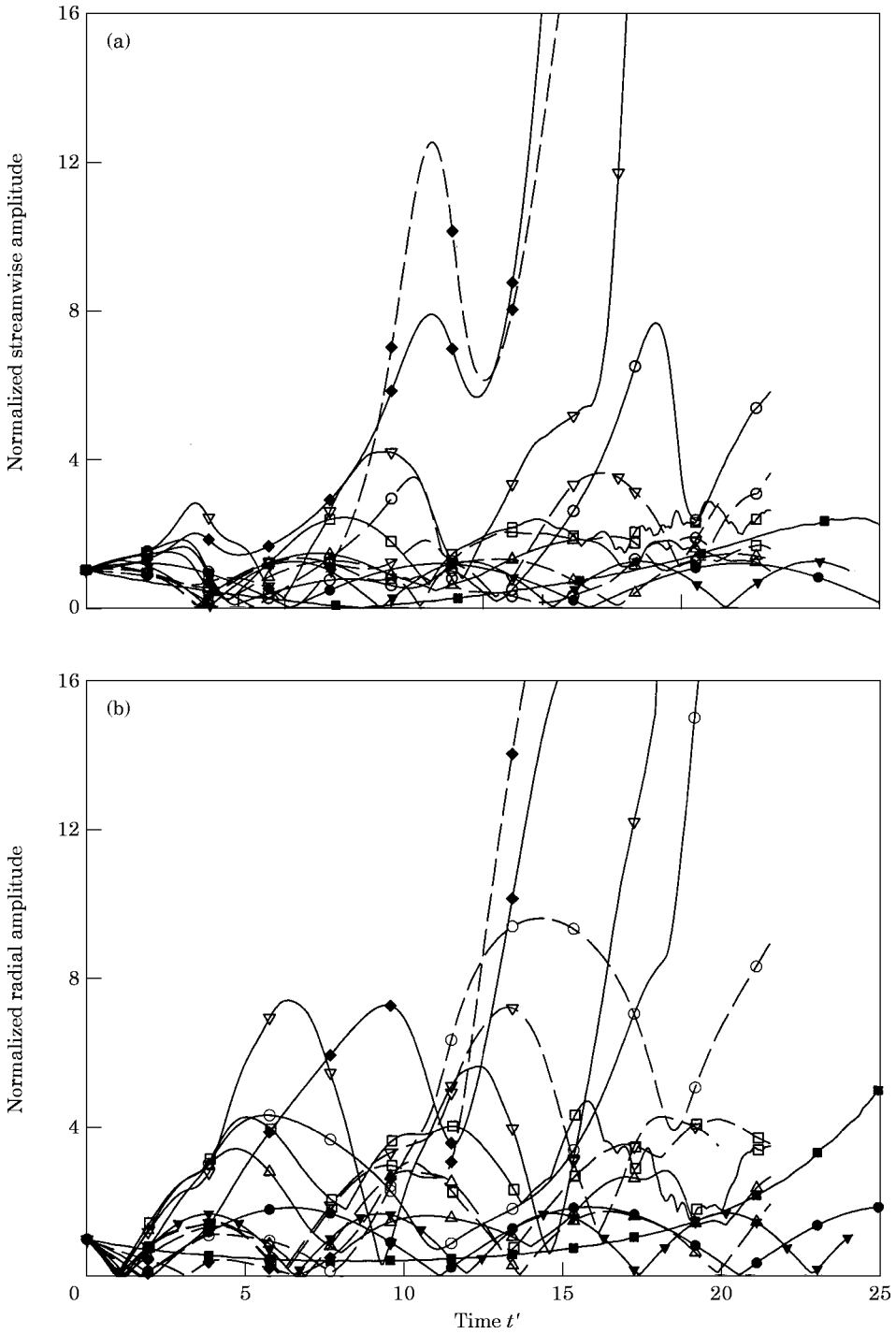

Figure 18. Normalized amplitudes of interacting vortex rings. (a) Streamwise; (b) Radial. Single vortex: ●, $m = 2$; ▼, $m = 5$; ■, $m^* = 8$. ◆, $m = 1$; ○, $m = 2$; △, $m = 3$; □, $m = 4$; ▽, $m = 5$. ———, Initially trailing vortex; ·····, initially leading vortex.

start of its evolution, while the radial amplitude starts to increase continuously, at $t' \approx 6$. No periodicity is found. At this $t' \approx 6$, the corresponding streamwise amplitude is about 1·8. At the wavenumber immediately higher than the unstable mode wavenumber, the maximum streamwise amplitude, which again is periodic, is about 1·3. For higher wavenumbers, the maximum streamwise amplitude is again unity and periodic. The findings of Knio and Ghoniem [23] seem to suggest that for a single vortex the critical streamwise amplitude seems to be about 1·8, beyond which the radial amplitude starts to grow continuously, while the streamwise perturbation grows continuously only during the final stage of its evolution.

At the unstable mode of $m^* = 8$ of a single vortex ring of the present parameters, the amplitudes in both directions indicate their continuous increases a $t' > 10$ (Figure 18). The critical streamwise amplitude seems also to be about 1·8 at $t' \approx 21$, agreeing with that of Knio and Ghoniem [23].

For the interacting perturbed vortices the streamwise and radial amplitudes of the initially leading and trailing vortices are also shown in Figures 18a and 18b. Both peak amplitudes of the trailing vortex are always higher than the corresponding ones of a single vortex ring of the same wavenumber, such as those of $m = 2$. The leading vortex, however, may be higher or lower in both peak amplitudes, depending on the slip through and wavenumber. The above phenomenon indicates that the effect of interaction on the evolution of the trailing vortex will result in bigger perturbations in both the streamwise and radial directions.

At $m = 5$ of the present two interacting vortex rings, the continuous increase in the peak amplitude of the streamwise perturbation of the initially trailing vortex during the three slip throughs, as mentioned above, is clearly shown in Figure 18a. The rapid continuous increase in the streamwise amplitude, which is different from that of a single vortex, and of the radial amplitude $t' > 16$ of the third slip through suggest the critical streamwise amplitude for interacting vortices is about 5, beyond which the exponential growth and unstable mode are found (Figure 18a).

By adopting the above normalized streamwise amplitude as the criterion for the unstable mode to occur, the peak streamwise amplitudes of the trailing vortex at wavenumbers $m = 3$ and 4 are lower than 5. This may explain the linearly stable mode of these interacting vortices as observed above. For $m = 2$, at $t' \approx 17{\cdot}4$ the streamwise amplitude of the trailing vortex (initially trailing vortex) during the third slip through reaches a value of 5. Thus, one might expect the onset of the unstable mode. Study of the shape of the trailing vortex at $t' = 19$ (Figure 10d) indicates that on the xy-plane the trailing vortex, while slipping through the outer leading vortex, is fairly sharply curved and is similar to the early formation of hairpin vortices of the unstable mode of $m = 5$ of the present interacting vortices and of single vortex of Knio and Ghoniem [23]. At $t' = 20$ (not shown here) there is the presence of waves of higher wavenumber, nearest to the outer leading vortex. The cause for the damping of the unstable mode may be due the relative evolution or rotation of the two vortices and that during the third slip through, the two interacting vortices are normal to each other (Figure 10d). Because of the significant change in the shape of the trailing vortex (initially trailing vortex), especially in the minor axis, during the slip through, the effect of mutual induction is reduced, only resulting in its continuous growth of the radial perturbation (Figure 18b).

For $m = 1$, Figure 18a also shows that the criterion of normalized streamwise amplitude of the trailing vortex (initially leading vortex) is exceeded, even during the second slip through. Its growth, both the streamwise and radial, is damped down after the second slip through instant. However, the trailing vortex (initially leading vortex) has large tilt at the slip through instant (Figure 6c). The eccentricity and the reduced effect of mutual induction

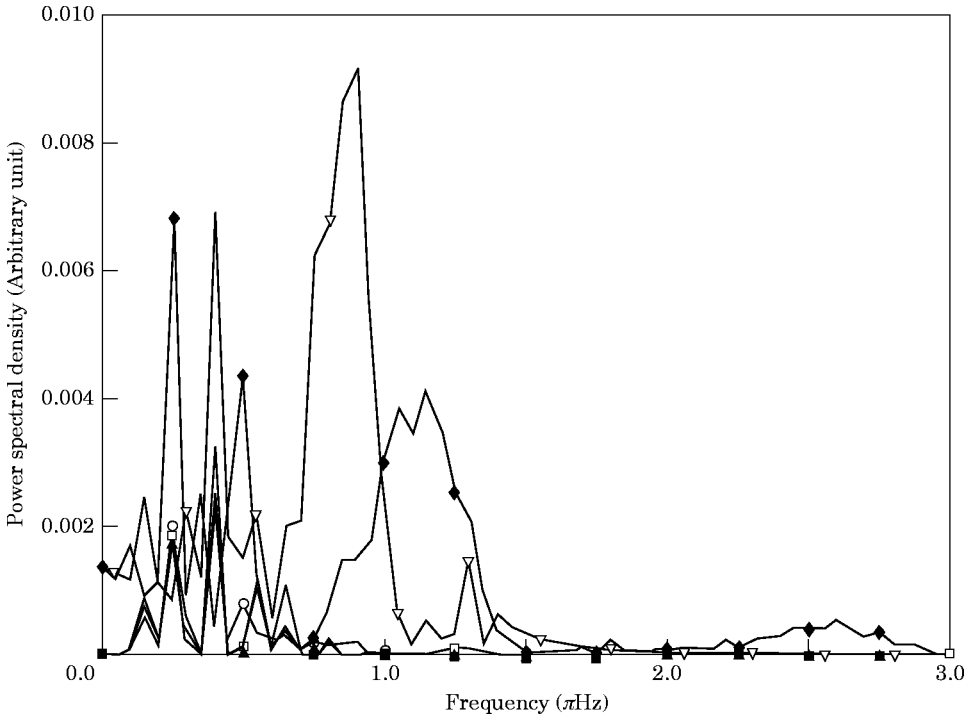

Figure 19. Spectra of sound pressure of major lobe at different wavenumbers. ●, $m = 0$; ◆, $m = 1$; ○, $m = 2$; △, $m = 3$; □, $m = 4$; ▽, $m = 5$.

may also be the causes for the absence of continuous growth. During the third slip through, the relative displacement of the two vortices and the mutual induction of the leading vortex (initially leading vortex) on the adjacent portions of the trailing vortex (initially trailing vortex) are responsible for its severe distortion with its long "tail" (Figure 6d) and the exponential growth (Figure 18). This is similar to the trailing vortex of the third slip through of $m = 5$ (Figure 15d). This also seems to suggest that the evolution of the two vortices of $m = 1$, because of their mutual induction, is also of unstable mode during the third slip through.

The above observations of the evolution of the trailing vortex of the wavenumbers $m = 1$ and 5 indicate the validity of the criterion of the normalized streamwise perturbation of about 5, beyond which unstable mode occurs. This lowering of the unstable mode wavenumber of a single vortex is due to the effect of interaction and their mutual induction. It is highly dependent on the wavenumber. This observation is expected as the stability of the wave of a single vortex ring depends strongly on the velocity and strain field induced by the ring on the perturbation [23]. With the presence of another vortex ring, the additional induction affects the velocity and strain field during their interaction, and thus the stability of the interacting vortices. This additional effect appears more significant on the trailing vortex as it is slipping through the outer leading vortex. With no perturbation, the trailing vortex has nearly six times higher streamwise velocity than its radial velocity and 5·5 times the streamwise velocity of the leading vortex (results not shown here). The higher velocity and strain field on the trailing vortex during interaction is responsible for its susceptibility to instability.

As shown in Figure 4, the above unstable perturbations of $m = 1$ and 5 during the third slip through are associated with high far field sound radiated on the major and minor lobes.

These higher sound pressures are of higher frequency and are found just before, during and after the third slip through instant. Because of the change to stable condition for that of $m = 2$, the increase in the sound radiated is not as significant as those of the other two wavenumbers. Thus, for $m = 0$, 2, 3 and 4, the sound pressure spectra of the major lobe are basically the same (Figure 19). However, for $m = 1$, the contribution from the subharmonic is more dominant and that from the harmonics, in the form of a broad peak, is also significant. For $m = 5$, the unstable mode results in higher spectral levels and the broad peak of the first harmonic is the most dominant. This phenomenon indicates that at the unstable wavenumber the sound pressure is dominated by the contributions from the ''broad'' peak of the first harmonic and the high frequency components are the main sources of far field sound radiated. This correlation of the unstable mode with the far field sound radiated indicates the effect of the wavenumber of the perturbation on the stability and on the sound radiated. It also indicates the effect of interaction on the two perturbed vortices and the occurrence of instability at lower wavenumber than that of a single vortex ring.

REFERENCES

1. A. B. C. Anderson 1956 *The Journal of the Acoustical Society of America* **28**, 914–921. Vortex-ring structure-transition in a jet emitting discrete acoustic frequencies.
2. H. A. Becker and T. A. Massaro 1968 *Journal of Fluid Mechanics* **31**, 435–448. Vortex evolution in a round jet.
3. J. E. Bridges and A. K. M. F. Hussain 1987 *Journal of Sound and Vibration* **117**, 289–311. Roles of initial condition and vortex pairing in jet noise.
4. A. K. M. F. Hussain 1983 *Journal of Fluid Mechanics* **173**, 303–356. Coherent structures and turbulence.
5. H. E. Fiedler 1988 *Progress in Aerospace Science* **25**, 231–269. Coherent structures in turbulent flows.
6. P. A. Jacobs and D. I. Pullin 1985 *Physics of Fluids* **28**, 1619–1625. Coalescence of stretching vortices.
7. S. K. Tang and N. W. M. Ko 1996 *Journal of Sound and Vibration* **187**, 287–310. On sound generated from the interaction of two inviscid coaxial vortex rings moving in the same direction.
8. H. Yamada and T. Matsui 1979 *Physics of Fluids* **22**, 1245–1249. Mutual slip-through of a pair of vortex rings.
9. Y. Oshima, T. Kambe and S. Asaka 1975 *Journal of the Physical Society of Japan* **38**, 1159–1166. Interaction of two vortex rings moving along a common axis of symmetry.
10. A. K. M. F. Hussain and A. R. Clark 1981 *Journal of Fluid Mechanics* **104**, 263–294. On the coherent structure of axisymetric mixing layer: a flow-visualization study.
11. A. Powell 1964 *The Journal of the Acoustical Society of America* **36,** 177–195. Theory of vortex sound.
12. W. Möhring 1978 *Journal of Fluid Mechanics* **85**, 685–691. On vortex sound at low mach number.
13. J. E. Ffowcs Williams and A. J. Kempton 1978 *Journal of Fluid Mechanics* **84**, 673–694. The noise from large scale structure of a jet.
14. V. Kibens 1980 *American Institute of Aeronautics and Astronautics Journal* **18**, 434–441. Discrete noise spectrum generated by an acoustically excited jet.
15. T. Kambe and T. Minota 1981 *Journal of Sound and Vibration* **74**, 61–72. Sound radiation from vortex systems.
16. J. Laufer and T. Yen 1983 *Journal of Fluid Mechanics* **134**, 1–31. Noise generated by a low-Mach-number jet.
17. S. K. Tang and N. W. M. Ko 1993 *Transactions of the American Society of Mechanical Engineers*, *Journal of Fluids Engineering* **115**, 425–435. A study of the noise generation mechanism in a circular air jet.
18. D. I. Pullin 1992 *Annual Review of Fluid Mechanics* **24**, 89–115. Contour dynamics methods.
19. S. E. Widnall and J. P. Sullivan 1973 *Proceedings of the Royal Society of London*, **A332**, 335–353. On the stability of vortex rings.

20. A. J. Yule 1978 *Journal of Fluid Mechanics* **89**, 413–432. Large-scale structure in the mixing layer of a round jet.
21. P. E. M. Schneider 1980 *Zeitschrift für Flugwissenschaften und Weltraumforschung* **4**, 307–318. Sekundärwirbelbildung bei ringwirbeln und in freistrahlen.
22. C. O. Paschereit, D. Oster, T. A. Long, H. E. Fiedler and I. Wygnanski 1992 *Experiments in Fluids* **12**, 189–199. Flow visualization of interactions among large coherent structures in an axisymmetric jet.
23. O. M, Knio and A. F. Ghoniem 1990 *Journal of Computational Physics* **86**, 75–106. Numerical study of a three-dimensional vortex method.
24. K. Shariff, R. Verzicco and P. Orlandi 1994 *Journal of Fluid Mechanics* **279**, 351–375. A numerical study of three-dimensional vortex ring instabilities: viscous corrections and early non-linear stage.
25. R. Wille 1963 *Zeitschrift für Flugwissenschaften* **11**, 222–233. Beiträge zur phänomenologie der freistrahlen.
26. G. K. Batchelor 1967 *An introduction to Fluid Dynamics*. Cambridge University Press.
27. D. W. Moore and P. G. Saffman 1972 *Philosophical Transactions of the Royal Society of London*, **A272**, 403–429. The motion of a vortex with axial flow.
28. P. G. Saffman 1992 *Vortex Dynamics*. Cambridge University Press.
29. G. Winckelmans and A. Leonard 1993 *Journal of Computational Physics* **109**, 247–273. Contributions to vortex particle methods for the computation of three dimensional incompressible unsteady flows.
30. G. Pedrizzetti 1992 *Fluid Dynamics Research* **10**, 101–115. Insight into singular vortex flows.
31. J. E. Bridges 1990 *Ph.D. Thesis*, *University of Houston*. Application of coherent structures and vortex sound theories to jet noise.
32. M. R. Dhanak and B. De Bernardinis 1981 *Journal of Fluid Mechanics* **109**, 189–216. The evolution of an elliptic vortex ring.
33. A. Ghosh, J. Bridges and F. Hussain 1995 *Transactions of the American Society of Mechanical Engineers*, *Journal of Vibration and Acoustics* **117**, 172–179. Instantaneous directivity in jet noise by multiple decomposition.
34. A. Michalke and H. V. Fuchs 1975 *Journal of Fluid Mechanics* **80**, 179–205. On turbulence and noise of an axisymmetric shear flow.
35. J. C. Lasheras, A. Lecuona and P. Rodriguez 1991 *Lectures in Applied Mathematics* **28**, 403–422. Three-dimensional vorticity dynamics in the near field of coflowing forced jet.
36. F. K. Browand and J. Laufer 1975 *Proceedings of the Fourth Biennial Symposium on Turbulence in Liquids*, *Missouri-Rolla*, 333–344. The role of large scale structures in the initial development of circular jets.